A general method to generate artificial spike train populations matching recorded neurons

Samira Abbasi[1] · Selva Maran[2] · Dieter Jaeger[2]

Abstract

We developed a general method to generate populations of artificial spike trains (ASTs) that match the statistics of recorded neurons. The method is based on computing a Gaussian local rate function of the recorded spike trains, which results in rate templates from which ASTs are drawn as gamma distributed processes with a refractory period. Multiple instances of spike trains can be sampled from the same rate templates. Importantly, we can manipulate rate-covariances between spike trains by performing simple algorithmic transformations on the rate templates, such as filtering or amplifying specific frequency bands, and adding behavior related rate modulations. The method was examined for accuracy and limitations using surrogate data such as sine wave rate templates, and was then verified for recorded spike trains from cerebellum and cerebral cortex. We found that ASTs generated with this method can closely follow the firing rate and local as well as global spike time variance and power spectrum. The method is primarily intended to generate well-controlled spike train populations as inputs for dynamic clamp studies or biophysically realistic multicompartmental models. Such inputs are essential to study detailed properties of synaptic integration with well-controlled input patterns that mimic the *in vivo* situation while allowing manipulation of input rate covariances at different time scales.

Keywords Synaptic · *In vivo* · Cerebellum · Cortex · Model · Correlation

Abbreviations

aGLR	Adaptive Gaussian Local Rate template
saGLR	Rate scaled adaptive Local Rate template
AST	Artificial Spike Train
CV	Coefficient of Variation
u	u-fold increase of aGLR rate within single computed ISI (real valued number)
ISI	Inter-spike Interval
LV	Local Variation
MF	Mossy fiber
MT	Middle temporal area pyramidal neuron
PC	Purkinje cell
PETH	Peri Event Time Histogram
SF	Shift Fraction
sGLR	Slow Gaussian Local Rate template

Action Editor: Alain Destexhe

✉ Dieter Jaeger
djaeger@emory.edu

[1] Department of Biomedical Engineering, Hamedan University of Technology, Hamedan 65169-13733, Iran

[2] Department Biology, Emory University, Atlanta, GA 30033, USA

1 Introduction

To understand neural coding in behaving animals requires large scale network theories and models, but also a good understanding of synaptic integration in single neurons, as nonlinear neural properties can have significant impact on network processing (Silver 2010). For example, synaptic input can have an additive or gain modulating (Brown et al. 2014; Murphy and Miller 2003) function, and spike threshold nonlinearities can create nonlinear interactions between signal and noise inputs (Lyamzin et al. 2015). To gain a better understanding of synaptic integration in each type of neuron it is important that one can study it with synaptic input conditions that closely mimic the situation in a behaving animal, as synaptic integration can be dramatically non-linear and depend on specific input conditions, such as coincident inputs (Edgerton et al. 2010; Mel 1993), or inputs to specific part of a dendrite (Ledergerber and Larkum 2010; Major et al. 2013; Poirazi et al. 2003; Polsky et al. 2009). To systematically study these effects and gain a functionally relevant understanding of neural input-output transfer functions it is therefore necessary to apply controlled but realistic patterns of inputs to the type of neuron in question, either *via* dynamic clamp *in vitro*, or to a

biophysically realistic neuron model. The gold standard of a realistic input pattern is, of course, the actual input pattern received by a neuron in a behaving animal. Unfortunately, such input patterns cannot be measured directly. Whole cell recordings in behaving animals may provide the closest approximation to such measurements, but do not completely disambiguate inhibition & excitation, nor completely separate synaptic currents from voltage-gated currents due to severe space clamp limitations. Extracellular single unit recordings from large populations of neurons are becoming more common for example using the Neuropixels probe (Jun et al. 2017), but cannot identify a population of neurons converging onto any given target neuron. Therefore, in the study of how complex *in-vivo* patterns of inputs are integrated in model neurons, the generation of artificial spike trains (ASTs) that can most closely mimic *in vivo* conditions while allowing the flexibility of controlling correlation structure between inputs is essential.

A number of mathematical algorithms have been previously developed to generate ASTs with specific correlation structures. These algorithms are based on a variety of statistical techniques, including general linear models (Pillow et al. 2008), a mixture of Poisson spike trains or doubly stochastic processes (Brette 2009; Krumin and Shoham 2009), multivariate Gaussian models (Gutnisky and Josic 2010; Lyamzin et al. 2010; Macke et al. 2009) or maximum entropy with a Markovian assumption (Marre et al. 2009). Using these algorithms, pairwise and higher order correlation structures can be precisely specified. As experimentalists we were interested though to more closely condition a set of ASTs on a population of recorded neurons. Specifically a goal was to replicate slow rate changes within and shared between spike trains (Cao et al. 2017), as well as detailed Interspike-interval statistics including a refractory period, as well as global (coefficient of variation (CV)) and local (local variation (LV) spike time variability. Further, we wanted to flexibly insert recorded behavioral-related spike rate modulations into subpopulations of ASTs. Towards these goals, we developed an algorithm based on constructing and manipulating rate templates of recorded neurons and generating gamma-distributed random processes with a refractory period from these rate templates. Our initial use of this algorithm was recently published in a study modeling the processing of Purkinje cell input by the cerebellar nuclei for respiratory related behavioral coding (Abbasi et al. 2017). Here we further refine this algorithm and test it with surrogate data to determine its accuracy and limitations. We then show that we can reproduce spike train properties of different types of recorded neurons, specifically cortical pyramidal cells as well as cerebellar Purkinje cells and mossy fibers.

2 Methods

2.1 Biological data base of recorded spike trains

Our method of generating AST populations is aimed at replicating the spike train statistics of specific extracellular recordings from behaving animals and to control rate change correlations between ASTs. The purpose is to apply these ASTs as input populations to neural simulations or use them to construct dynamic clamp input conductances for the study of synaptic integration of complex input patterns *in vitro*. Recorded spike trains are becoming increasingly available through on-line databases such as crcns.org. We took one of our test cases from area MT recordings in the behaving primate (Cui et al. 2013) from this database https://crcns.org/data-sets/vc/mt-1/about. Our other test cases of cerebellar mossy fiber and Purkinje cell recordings from awake mice were taken from our own previous study in collaboration with Detlef Heck's lab at University of Tennessee Health Sciences Center (Abbasi et al. 2017). Together these test cases span a wide range of spontaneous firing rates as well as spiking patterns. Figure 1 shows the Purkinje cell as an example of which statistical properties we extract from these spike trains. These include spike rate fluctuations (Fig. 1a), the interspike-interval (ISI) distribution (Fig. 1b), the power spectrum (Fig. 1c), and the statistical measures of global ISI variance (CV):

$$C_V = \sqrt{\frac{1}{n-1}\sum_{i=1}^{n}\left(T_i - \overline{T}\right)^2 / T} \tag{1}$$

as well as local ISI variance (LV). The LV is calculated from the variability of 2 successive intervals as:

$$L_V = \frac{1}{n-1}\sum_{i=1}^{n-1}\frac{3(T_i - T_{i+1})^2}{(T_i + T_{i+1})^2} \tag{2}$$

For a Poisson spike train with a CV of 1, the LV is also 1 (Shinomoto et al. 2003), and for a regular spike train with equal ISIs both measures are 0. Most recorded spike trains are non-stationary due to temporal varying rates, however, and the CV will increase as a result of spike rate variability while the LV does not (Shinomoto et al. 2005). A particular advantage of the LV is that the expected LV of a gamma process with shape parameter κ can be mathematically derived as:

$$\langle L_V \rangle = \frac{3}{2\kappa + 1} \tag{3}$$

(Shinomoto et al. 2005) We note in agreement with previous studies (Miura et al. 2006; Pipa et al. 2013) that the ISI

distribution of recorded spike trains often fits a gamma distribution quite well, though some systematic differences can be detected as well (Fig. 5).

2.2 Generation of ASTs

The general outline of our AST generating algorithm follows 4 steps:

1) Create a rate template from a recorded spike train. We perform this step by convolving spike times with Gaussians in a 2 step process as described below.
2) As desired, perform algebra on the rate template to blend different temporal profiles such as oscillations, change the mean rate, or gain-scale rate modulations.
3) As desired, convolve the rate template with a much shorter waveform template with mean 1 at a sequence of event times. Typically, the short template represents a recorded peri-stimulus time histogram for a specific sensory or motor event and is convolved into the template at such behavioral event times.
4) Create ASTs as gamma processes with an added absolute refractory period by drawing ISIs with a time-varying mean rate taken from the final rate template and a shape factor κ calculated from the Lv of the recorded spike train. ASTs can be created from any mix of rate templates created in steps 2 and 3.

2.3 Step 1. Creating an adaptive Gaussian rate template from recorded spike trains as an estimator of the instantaneous rate function

Recorded spike trains frequently contain some contamination of noise spikes that fall into the absolute refractory period of the neuron. We first remove ISIs smaller than the absolute refractory period by removing the 2nd spike of such intervals. As we will show in the Results, an optimal refractory period can be estimated by finding the value (in ms) that leads to minimal errors in the ISI distribution from ASTs compared to the recorded spike train. We find optimal values for the refractory period of each spike train by employing a particle-swarm optimization algorithm, which resolves to a value of 5 ms for all 3 cell types we tested (see Results). We then construct a 'slow' Gaussian local rate template (sGLR) from this spike train (Fig. 2a) by convolving all spikes with a Gaussian using a width parameter σ of 100 ms (Fig. 2b). Convolving spike trains with Gaussians results in a continuous function with a low-pass filtered estimate of the instantaneous spike rate and a mean value of the mean spike rate (Paulin and Hoffman

2001). We then create a 2nd GLR with a narrower Gaussian filter with a width σ given as:

$$\sigma = \frac{1}{\sqrt{2\pi}*rate*scale} \tag{4}$$

In Eq. (4), The scale parameter is a free parameter scaling σ in relation to the time-varying spike rate (rate) of the sGLR. The optimal Gaussian σ, *i.e.* the value yielding the most information for each spike in the GLR, is a function of mean rate and also the CV of the spike train to be rate-coded (Paulin and Hoffman 2001). It comes to about twice the average ISI for a CV of 1, and 0.03 of the average ISI for a CV of 0.01 (Paulin and Hoffman 2001). We find optimal values for the scale factor for each spike train by employing a particle-swarm optimization algorithm, which resolve to values between 0.12 and 0.146 for our 3 cell types tested (see Results). By using σ dependent on the instantaneous rate of our sGLR we create an 'adaptive' Gaussian local rate function (aGLR) where narrower Gaussians are used when the spike rate gets faster to map individual spike times more accurately in the rate function (Fig. 2b black trace).

2.4 Step 2

Our method extensively utilizes the ability to manipulate rate templates prior to AST generation in order to result in distinct types and strengths of rate correlations between different ASTs. First, we normalize the aGLR to a mean of 1.0. In order to control the overall amount of synchronous rate coding in the population of ASTs that are generated as an input to a single cell simulation or a dynamic clamp stimulus, we perform the following manipulation: First, a proportion (synchronous fraction) of ASTs are pulled from the identical rate template. Second, the remaining ASTS (shifted fraction) are generated by a random time shift between <min> and < length of template> along a circle, where <min> can be specified as a minimal required time shift. ASTs generated from different shifted versions will result in spike trains with identical statistical properties but generally without synchronous rate changes at time delays smaller than <min>, though they will individually have a very high rate cross-correlation at a delay of <shift time>.

Additionally, we have implemented the ability to gain-scale rate changes in a flexible way. First, we can scale an entire aGLR by multiplication with a gain factor. Or second, we can only gain-scale a certain frequency component of the aGLR by creating a filtered version and after removing it from the original aGLR multiplying the filtered version by the gain factor and multiplying it back in. This second method can for example be used to dampen a certain low frequency band in the rate template (Fig. 3a, b) or to amplify another band

Fig. 1 AST targets. **a** Adaptive Gaussian Rate template from a 10s Purkinje cell spike train (see Fig. 2 for construction process). **b** Interspike-Interval (ISI) histogram of Purkinje cell recording (7474 spikes see Table 1). Spike density is calculated as spikes per bin per second. **c** Power spectrum of Purkinje cell spike train
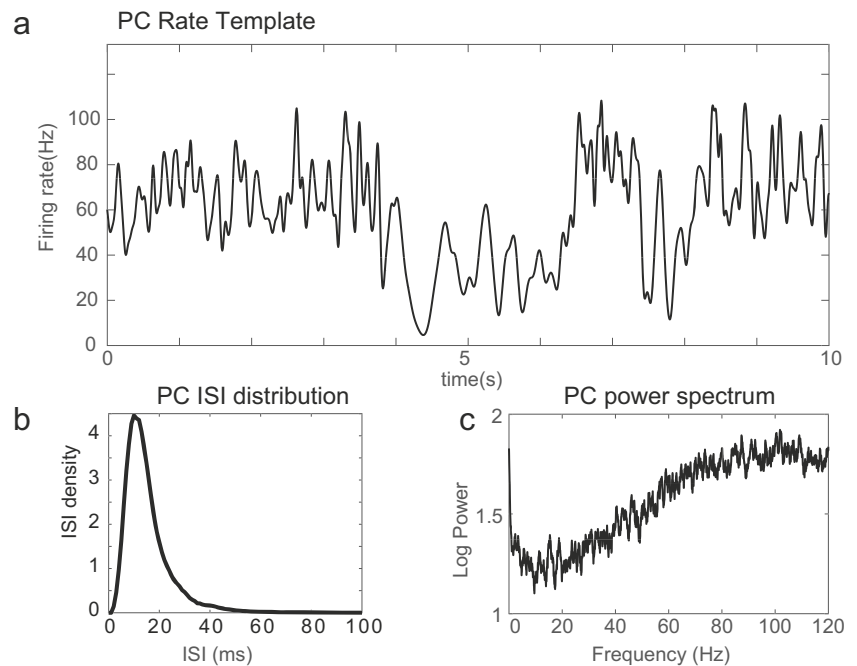
such as beta oscillations (Fig. 3c, d). An oscillatory or noise component could also be multiplied into the normalized aGLR. Starting with recorded spike trains from awake behaving animals as a blueprint, these rate template manipulations allow researchers to generate a wide range of biologically relevant variations of artificial synaptic input patterns that can be applied to biophysical neuron models or with dynamic clamp to recorded neurons.

2.5 Step 3

In many experimental studies subsets of neurons show specific rate changes associated with sensory, motor, or cognitive

events that ensue in a controlled behavior. The average of these rate changes is commonly described by a peri-event time histogram (PETH). We normalize any PETH to 1.0 and detrend it by regressing out any linear component in the rate change across the entire spike train. Detrending results in a rate function starting and ending with a value of 1.0, which is important to avoid sudden rate changes in our time-shifted rate functions. We then can apply a gain-scale factor to the normalized detrended PETH to amplify or diminish behavioral rate modulations before convolving the final PETH rate function into the aGLR at the times of measured behavioral events or at intervals otherwise justified. The objective of this method is to create controlled fractions of behaviorally co-modulated

Fig. 2 Construction of adaptive Gaussian Rate Template **a** 5 s segment of spike train from area MT neuron, **b** Each spike (dotted vertical lines) is first convolved with a fixed width Gaussian and the Gaussians are summed up (green line, slow rate function). Then the slow rate template is used to determine an adapted width of a Gaussian for each spike to produce the adaptive rate template (see Methods for details)
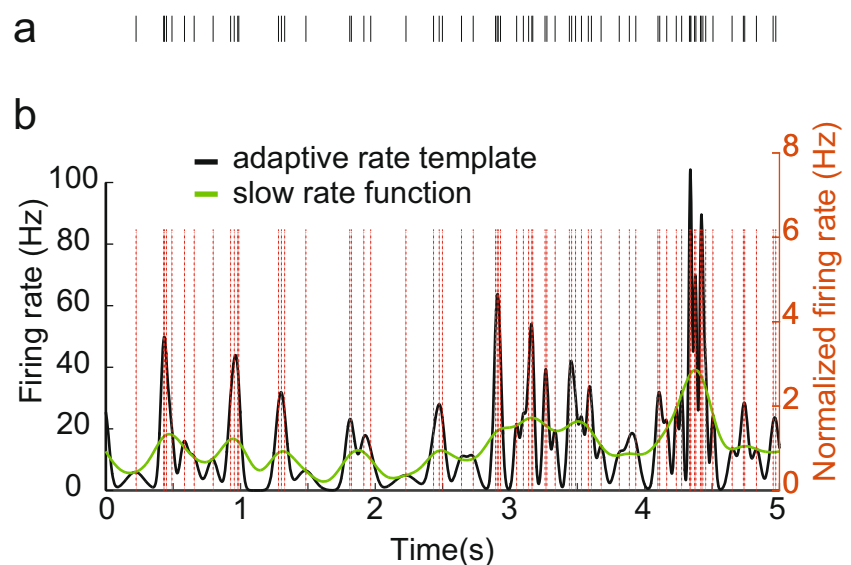
spike trains in the input to a biophysically detailed single cell model or to a dynamic clamp stimulus for slice recordings. This method enables us to flexibly scale the amplitude of behaviorally related rate changes as well as the fraction of inputs exhibiting such changes, thus exploring a fundamental dimension of the coding capacity of single neurons with respect to transmitting behaviorally relevant information in their output spike trains.

2.6 Step 4

Finally, we generate one or more ASTs from each final aGLR after all rate manipulations are performed. First the normalized aGLR is scaled back to the desired target mean spike rate, and this rate is further adjusted to account for the effect of refractory period subtraction in the generated gamma distribution, which results in our final rate scaled aGLR (saGLR). To replicate the original local variance of recorded ISIs, we draw gamma distributed ISIs with a shape factor κ computed from the LV of the recorded spike train by Eq. (3) above after subtracting the absolute refractory period (aRP) from each recorded ISI. The AST generation process starts at t = 0 by selecting a random gamma interval using the Matlab gamrnd() function for a mean rate of 1, and a regularity of κ. This gamma interval is then scaled by multiplying with the mean of the saGLR during this first interval in an iterative process (see our function singleASTgen() for details https://doi.org/10.15139/S3/8ILYHZ. Finally, the aRP is added back into to

this gamma distributed interval. (Note that the aRP is first taken out of the recorded spike train to create an estimate of κ for a gamma distribution matching the recording, then a gamma interval is sampled using this κ, and finally the aRP is added back to this interval). Now we place a spike at the end of this calculated interval (ISI1), and start the process over at time t1 = t0 + ISI1 to iterate this process until the end of the rate template is reached.

There are a couple of technical difficulties with this serial sampling of spike times, however. First, if the local spike rate drops to zero, the next gamma interval would be infinitely long. We therefore set a floor for our rate function below which the spike rate is not allowed to drop, typically a value of less than 1/20 of the mean spike rate. Second, when there are dramatic spike rate increases in the saGLR, an ISI picked at the time of a slow local spike rate may end up with a spike time that is placed well behind a time at which the saGLR had already increased manyfold. We solved this problem heuristically, by defining an ungamma factor u, which is given by an u-fold increase of the saGLR within any given gamma ISI. If such an -u-fold rate increase is found inside an ISI, a 2nd gamma interval is computed using the maximal rate encountered in the original ISI, and the final ISI is the sum of the first ISI truncated at the time of the u-fold rate increase plus the 2nd ISI. Such events were quite rare and indicated a clear nonstationarity in the rate function, which nonetheless can occur in neurons with pronounced bursts or strong behaviorally relevant activations (see Fig. 9c, f below for an example).
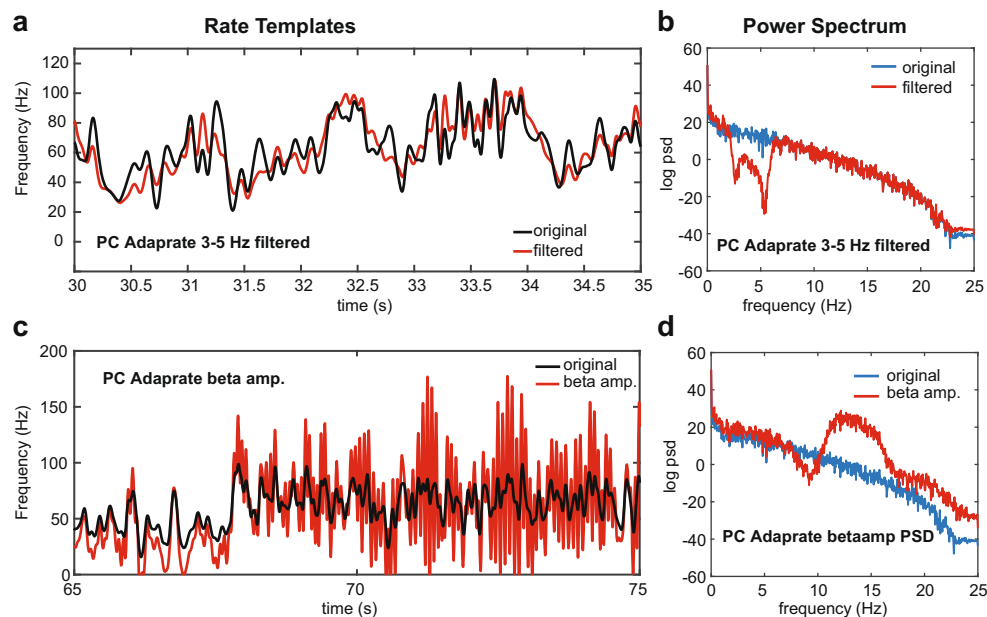
Fig. 3 Examples of rate template manipulations to control AST properties. **a** aGLR of a 5 s segment from a Purkinje cell recording (black) and a manipulated rate template (red) in which the 3–5 Hz frequency component has been reduced by applying a gain of 0.1 to this frequency band (for details see our Matlab function splitsignal_adjust() at https://doi.org/10.15139/S3/8ILYHZ. **b** Power spectrum of the original rate template and the 2–5 Hz filtered template. Data are from a 115 s template. **c** aGLR from a 10 s segment of the same Purkinje cell recording (black) and a manipulated rate template (red), in which a beta frequency band (12–16 Hz) was amplified by a gain factor of 20. **d** Power spectrum of beta-band amplified rate template. Data are from a 115 s template

2.7 Creating populations from controlled ensembles of aGLRs

Following these steps, we generate a population of ASTs as needed for inputs to a simulation or a dynamic clamp experiment. To control for correlations between inputs we generate populations of ASTs in which a specified fraction of ASTs is made from time-shifted templates as described in 2.4 above. We denote this fraction as shift fraction ($0 < SF < 1$). Similarly, we define a Behavioral Modulation Fraction as the fraction of aGLRs that are convolved with a PETH as described above under 2.5. With simple edits to the code, fractions of ASTs containing a specified oscillatory component, band-pass filtered versions of the aGLRs, or gain-scaled versions of the aGLRs can be generated. As we show below under Results, ASTs are statistically matched to the original spike trains, and in turn can be used themselves as sources for new aGLRs.

All Matlab code is available online https://doi.org/10.15139/S3/8ILYHZ as a toolkit to produce ASTs from user supplied spike trains.

3 Results

3.1 Determining the match of ASTs with the properties of recordings for 3 types of neurons

The goal of our AST generating algorithm is to create ASTs with statistics that match the original recorded spike trains while allowing flexible manipulations in their population properties like rate-correlations and behavioral modulation strength. We used 3 types of neurons with very different firing patterns as our test cases (Fig. 4). A cerebellar Purkinje cell (PC) recorded in an awake mouse (Abbasi et al. 2017; Cao et al. 2017) with a fast mean spike rate of 64.8 Hz and a moderate CV of 0.67 while maintain high local regularity ($LV = 0.3$); a cerebellar mossy fiber (MF) from the same study with a slower rate and less regular firing; and an area MT recording from primate visual cortex taken from an online database (https://crcns.org/data-sets/vc/mt-1/aboutcell 42) with a slow firing rate of 6.3 Hz and very high CV of 1.6 (Table 1). For all test cases, we found that our ASTs resemble locally randomized versions of the original spike trains (Fig. 4a–c). We computed the mean rate, CV, and LV of 100 ASTs sampled from cell's template. All statistical outcomes were quite close to the original recorded spike trains, with mean spike rates within 1 Hz of the original, a CV difference of less than 0.02, and an LV difference of less than 0.01 for PC and MF recordings, while a somewhat bigger LV difference of 0.03 resulted for the MT neuron (Table 1). We then compared the Gaussian rate template (aGLR) constructed from the original recordings (Fig. 4d–f, black traces) to the mean aGLR

computed from 100 ASTs drawn from the recorded aGLR (Fig. 4d–f, red traces). We found that the rate fluctuations in the recorded aGLR where maintained faithfully in the average aGLR of the ASTs, though the fastest rate changes appeared a bit attenuated (Fig. 4d–f: see slightly larger sharp peaks in black than in red traces). Finally, we compared the ISI distributions of the original spike trains to those of the derived ASTs (Fig. 4g–i). While there is a satisfactory match to a unimodal gaussian distribution in each case, we did find systematic differences that were more pronounced for the MF and MT neurons. Here the peak of the ISI distribution is shifted to the left for the ASTs by several ms, and diminished in amplitude. These shapes of the gamma distributions of the ASTs are forced by the shape parameter κ, which was chosen in order to reproduce the exact match of the LV of the original recordings. The ensuing small mismatch in ISI distributions does indicate that biological MF and MT spike trains may not be modeled perfectly with a gamma distribution with a stationary κ parameter. This could be addressed at least in part by taking κ from a time-varying k- template based on the recording, which would be an easy extension of our algorithm, but was not explored here.

3.2 Controlling partial rate correlations by creating mixed AST populations

As described in Methods (2.4) we use time-shifted versions of aGLRs to create populations of ASTs that contain a specific proportion of spike trains with synchronized rate changes (drawn from the non-shifted template) and the remainder is drawn from randomly time-shifted rate templates. We denote the fraction of spike trains that do not show synchronous rate changes as Shift Fraction (SF: 0–1). Here we show that the mean rate template computed from 100 ASTs matches the mean rate fluctuations of the original recording proportional to the SF used (Fig. 5). When 100 ASTs are drawn from the identical PC aGLR (SF = 0), the resulting average rate template from the ASTs matches the original PC recording (Fig. 5a). When 50 ASTs are drawn from the same aGLR, and 50 from time-shifted versions (SF = 0.5), the mean rate template computed from the 100 ASTs shows the rate fluctuations of the original template at 50% magnitude (Fig. 5b). Finally, when all 100 ASTs are drawn from time shifted aGLRs (SF =1), the resulting average rate template from ASTs do not show rate fluctuations related to the original waveform (Fig. 5c). Interestingly, the amplitude of the remaining random rate fluctuations is much smaller than rate fluctuations in recorded spike trains, suggesting that a neuron integrating such 100 independent inputs would not show the level of rate correlations observed in our *in vivo* recordings. Indeed, simultaneous *in vivo* recordings from Purkinje cells show large positive slow rate co-correlations, though only along the anterior-posterior (sagittal) axis (Cao et al. 2017). We replicated the analysis of
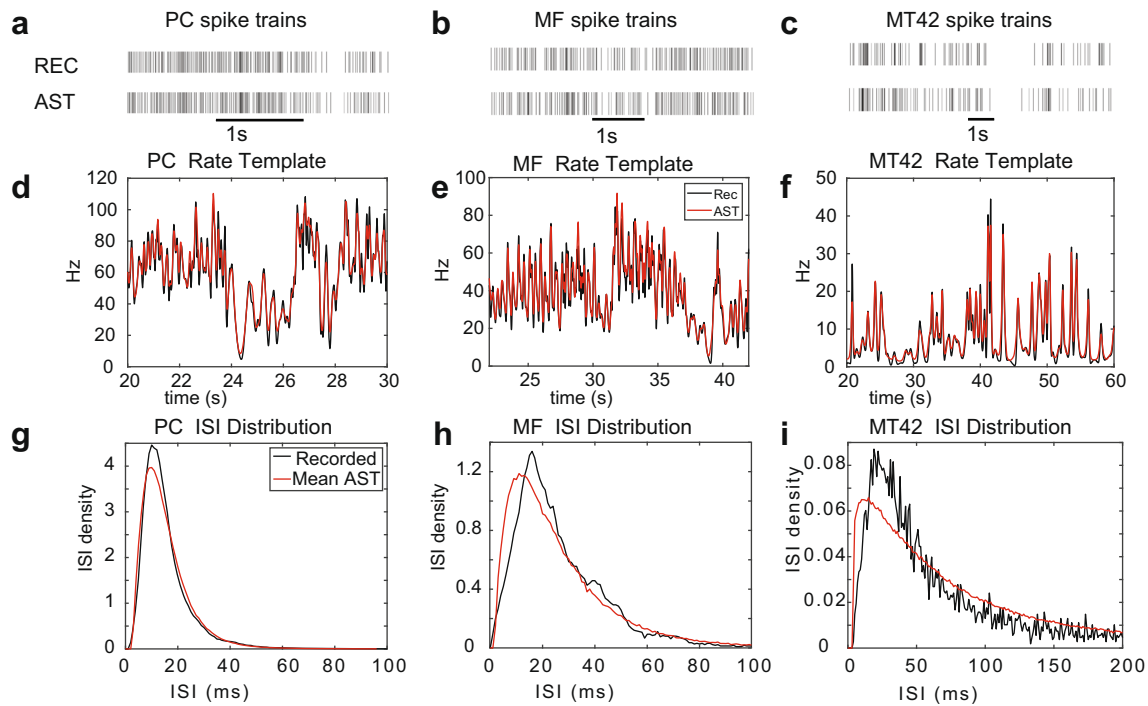
Fig. 4 Matching recorded spike trains to ASTs for PC, MF and MT neurons. **a–c** For each cell type a segment of spike data is shown from the recording (REC, top trace) and an AST generated from the aGLR of the recorded spike train. Note that the time base is different for each neuron based on their mean spike rate. **d–f** The aGLR is shown for a segment of the full template for the recording of each cell type (black trace), and superposed the average aGLR from 100 ASTs is depicted (red trace). **g–h** The ISI distribution of the full length recordings (PC: 115 s, MF: 45 s, MT42: 1079 s) and the mean ISI distribution of 100 ASTs of the same length (red). For these simulations, physiologically plausible assumptions were made about the free parameters of our search algorithm. See Table 3 for error comparison to other parameter settings

sliding window peak correlations employed by these authors (Fig. 5d–f), and find that our simulations with an SF of 0.5 show correlation coefficients roughly similar to pairs of sagittally aligned PCs. Therefore, our method of employing AST populations with rate correlations determined by an SF will allow us to carry out the generation of PC input patterns to DCN neuron simulations that match the population properties of *in vivo* PC recordings. We further suspect that modeling rate co-correlations as input to network or single cell simulations will be an important aspect for simulating activity in many areas of the brain. For example, recent evidence shows that simple measures of alertness such as pupil diameter, or motor state of an animal, are co-correlated with rate changes in almost all areas of cortex (Shimaoka et al. 2019; Stringer et al. 2019)

and even between cortex and cerebellum (Wagner et al. 2019). In our method, any global measure of activity changes (eg. pupil diameter, motor state) could be used as time varying factor multiplied into rate templates as a common rate change driver across ASTs.

3.3 Optimizing free parameters in the algorithm for creating best fits of AST statistics to original spike train

Our AST generation process has 4 parameters that need to be selected prior to running the template and AST generating algorithms. These parameters are the duration of the absolute refractory period (aRP), the value of the factor that scales the σ (Eq. (4)) to construct the aGLR, the lowest allowed spike rate (floor) in the aGLR, and finally the variable u determining at what u-fold rate increase of the aGLR within an AST ISI a selection of a shorter interval is triggered. For any given source spike train the settings of parameters that yields the closest matching ASTs to the original may differ. We explored the impact of these parameter for our 3 sample cell types.

First, we explored the error landscape of the AST performance of our three sample neurons (MF, PC, and MT) using a grid-search (Prinz et al. 2004) for all combinations of varying values for aRP (range 1–5 ms, increment 1 ms) and floor (range 0.05–1.95 Hz, increment 0.1 Hz). We plotted different

Table 1 Parameters (FR, CV, and LV) for recorded and mean of 100 ASTs from PC, MF, and MT #42 neurons

	FR (Hz)	CV	LV
Recorded PC	64.8	0.67	0.31
ASTs PC (mean ± SD)	65.2 ± 0.40	0.65 ± 0.017	0.30 ± 0.005
Recorded MF	36.5	0.80	0.46
ASTs MF (mean ± SD)	36.9 ± 0.57	0.809 ± 0.038	0.451 ± 0.016
Recorded MT 42	6.3	1.70	0.77
ASTs MT1 (mean ± SD)	6.9 ± 0.092	1.69 ± 0.044	0.74 ± 0.008
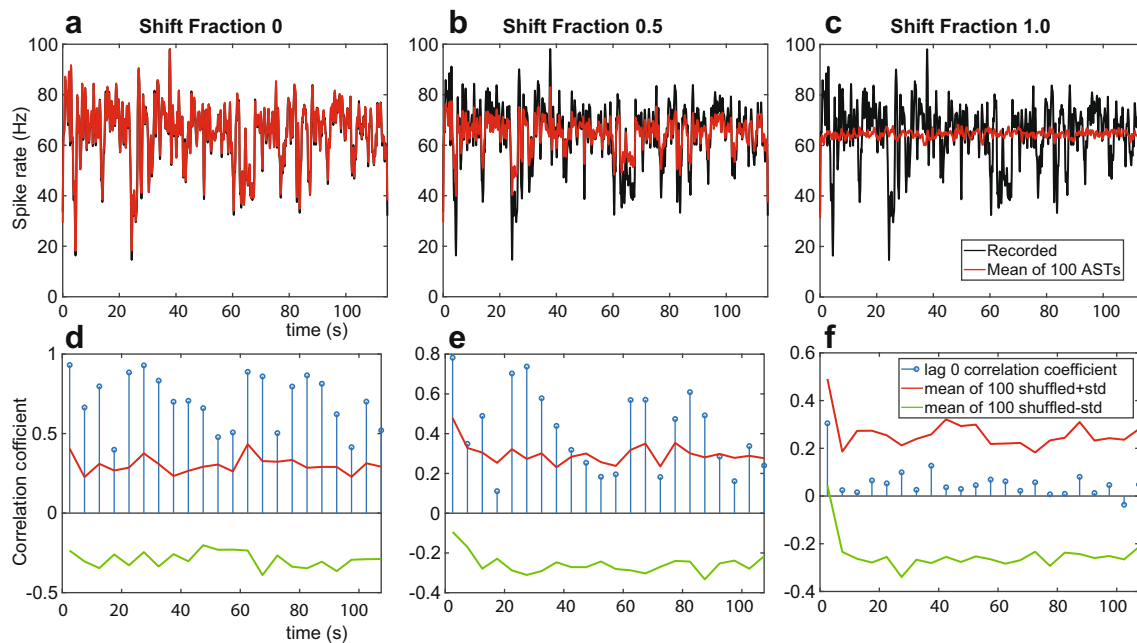
Fig. 5 Manipulating rate co-correlations within populations of ASTs. **a** The black trace shows the 'slow' rate template with a σ of 100 ms from the 115 s PC recording. The red traces show the average rate template also computed with a 100 ms σ from 100 ASTs where each AST was drawn from the same PC aGLR. **b** Same black trace, but 50 of the 100 ASTs for which the mean 'slow' rate template is shown (red) are drawn from a time-shifted version of the PC aGLR. **c** All 100 ASTs are drawn from time shifted aGLRs. **d**–**f** Average sliding window peak correlation at lag 0 between 'slow' rate templates computed for each AST and the rate template from the recording. Note that the correlations shown here are lower than they appear in panels **a**–**c** above because individual ASTs carry substantial individual fluctuations and are less correlated to the recording than the average rate template of all ASTs where these individual random fluctuations cancel out. Note that the sliding window correlation shows lower values at times when the rate change amplitude in the recording are lower as the noise-driven fluctuations in the AST rate at those times are relatively more dominant. The average peak correlation for an SF = 0 was 0.70, for SF = 0.5 was 0.41, and for SF = 1 was 0.05

error terms (Firing rate, CV, LV, ISI histogram error) as a percent deviation from the mean value found in the recording (Fig. 6). We found that for many parameter combinations the error surface was relatively flat. For example, for PC and MF the firing rate was generally not affected by the aRP or the floor (Fig. 6a1, b1). Nevertheless, each cell type showed a different profile of errors as a function of aRP and floor parameter settings The MT neuron showed a steeply increasing firing rate error with increasing floor factor (Fig. 6c1). The PC but not the MF shows a distinct influence of the aRP value on the final CV error of the ASTs, with a 4 ms aRP providing minimal error (Fig. 6a2). The CV error of the MT neuron in contrast was dominated by the effect of the floor factor (Fig. 6c2). This error was very large for small floor factors, showed a minimum at a value of 0.8 Hz, and then increased slowly. The ISI error remained the overall dominating error, as also seen in Fig. 4. However, for both the PC and MF it was a function of aRP (Fig. 6a3, b3), whereas for the MT neuron it was a function of both aRP and floor rate (Fig. 6c3). Interestingly, different error types show different minima in the choice of aRP and floor factors, and minimizing the total error (see below) therefore involves tradeoffs.

Next we ran a particle swarm global error minimization algorithm (Matlab particleswarm(), population size 20) with aRP, aGLR σ scale factor, floor, and u as free parameters. We specified lower and upper bounds on these parameters based on physiological plausibility. The aRP was limited between 1 and 5 ms, the σ scale factor between 0.1 and 2, the floor between 0.1 and 2 Hz, and the u-fold aGLR rate increase for aborting long ISIs between 2.0 and 10.0). We ran the particle swarm algorithm 3 times for each cell type, and calculated average errors for each sampled point in the 4-dimensional parameter space for 100 ASTs. The error that was minimized was the sum of the %deviation errors for firing rate, CV, LV, and ISI histogram (Table 3). We found consistent minimal errors between runs, despite some different final values for the parameter settings (Table 2), *i.e.* a single global minimum was not found, Nevertheless, for aRP, σ scale, and u parameters a relatively narrow range of solutions was found for all cells (Table 2). However, the floor parameter was poorly constrained for MF and PC, as also indicated by our grid search (Fig. 6a, b).

Because a global minimum was not found, we wondered how much of this failure could be attributed to the noise in our error measurements, and how much this error depended on the number of ASTs for which the error was averaged. In order to address this point, we calculated the %errors for rate, CV, LV, and ISI histogram, as well as the sum of these errors as total error, for populations of 2^n spike train for values of u between 0 and 9. We calculated the average and standard deviation of

errors for 100 repetitions of each population size. We found that for all cell types the mean total error was stable across population sizes but the standard deviation of the total errors for repeated measures was much higher for small AST populations sizes, and flattened out for population sizes above 100

(Fig. 6a4, b4, c4). For the average total error in 128 ASTs the standard deviation between measures was 0.27% for PC, 0.47% for MF, and 0.46% for MT, Therefore the different minima in total error found by repeated runs in our particle swarm algorithm for populations of 100 ASTs were within 1
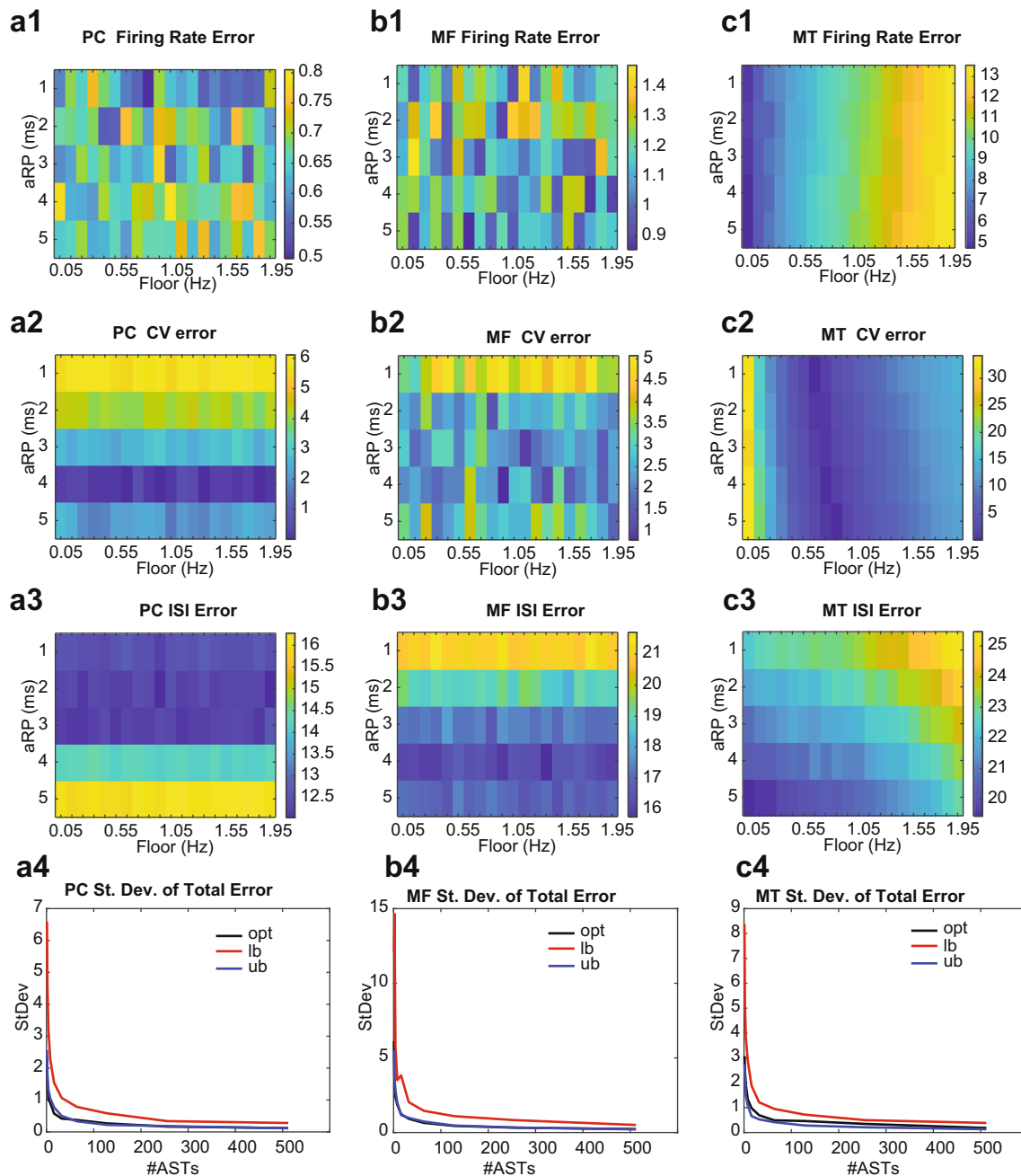
Fig. 6 Parameter search for best algorithm performance. abc1–3) For each cell type we plotted heat maps of the average percent error of 100 ASTs against the original recorded spike train for firing rate (FR), CV, and the average per bin deviation in the ISI density over 110 (PC), 150 (MF) or 200 (MT42) 1 ms bins starting at t = 0 ms ISIs (see Fig. 4). Note that the error ranges are quite different for different plots, and the color bar ranges are separately adjusted from min to max error for each plot. abc4) The standard deviation of the total error (rate + CV + LV + ISI errors) is shown

for different population sizes of ASTs for which these properties were averaged. AST populations of size were constructed 100 times, and the standard deviation between populations was calculated. As the total error was calculated as a % deviation from the mean of the recorded measures, a value for example of '2' in the StDev measurement denotes that the total error had a standard deviation of 2%. See Table 3 for the absolute size of the different errors

standard deviation of the measure (Table 2) and statistically indistinguishable.

3.4 Using constant rate templates as surrogate data to determine the ability to create spike trains with precisely defined rates and variance

To analyze the limitations in the ability of ASTs we produce to match specific features of spike trains we ran a suite of surrogate data designs. First, to study questions of how the spike rate affects quality of AST matches to templates, and whether matches of CV, LV, and rate with ASTs have any systematic error, we started with a simple test case, namely constant rate templates of 1 and 100 Hz. We drew 100 ASTs of 1000 s duration for the 1 Hz template, and 10 s duration for the 100 Hz template, with an expectation of an average of 1000 spikes per AST. We further drew ASTs with a target LV (calculating κ of the gamma process using Eq. (3)) of 0.1, which is a highly regular spike train, or 1.5, which is highly irregular. We found that for all conditions ASTs fit the target rate and LV with less than 1% error (Table 4). We computed an adaptive Gaussian rate template for each AST to depict the properties of the generated spike patterns (Fig. 7). A 1 Hz, 0.1 LV targeted AST resulted in fairly regularly placed single spikes (Fig. 7a), whereas a target LV of 1.5 resulted in highly irregular clustered spiking (Fig. 7b). Nevertheless, the average over 100 ASTs approximated the constant rate template accurately. The same observations held true for a 100 Hz constant rate template (Fig. 7c, d). We noted that the absolute firing rate error is not a function of spike rate, and remains at around 0.01 Hz for 0.1 LV spike trains, and 0.2–0.4 Hz for 1.5 LV spike trains if 100 ASTs are averaged. In contrast, the relation of the global rate variance (CV) to the local rate variance (LV) was rate dependent, and CV was higher for 1 Hz spike trains than 100 Hz spike trains (Table 4). This was likely an effect of

the added 4 ms absolute refractory period on the gamma distributed spike trains, which would regularize a 100 Hz spike train to a greater deal than a 1 Hz spike train.

3.5 Using zap templates as surrogate data to determine the ability to create spike trains following rate changes at different frequencies

Next, in order to determine how well ASTs generated with our rate template method can follow template rate changes at different frequencies we constructed sinusoidal rate templates with increasing frequency, which have also been called 'zap' stimuli and used to characterize resonances in intracellular recordings (Hutcheon and Yarom 2000). We tested different rate change frequencies with different target spike rates and values of LV. For quality of matching rate changes with ASTs we constructed single and averaged aGLRs from 100 ASTs (Fig. 8). For zap stimuli at 1–2 Hz with spike rates of 40–100 Hz we found that average aGLRs from 100 ASTs with an LV of either 0.1 (Fig. 8a) or 1.5 (Fig. 8c) could match the sinusoidal rate function well. The individual aGLR from single ASTs showed deviations from the target rate due to the noisiness of the gamma distributed spike trains, and these deviations increased with increasing LV as expected (Fig. 8a, c blue traces). As the zap sine frequency increased to 10 Hz (at t = 10s), the match of the average AST rate waveform (red) still matched the template (black), but small deviations started to occur, especially with an LV of 1.5 (Fig. 8b, d). When we decreased the spike rate to 10–20 Hz we found that an average aGLR can still match the 1–2 Hz target

Table 2 Particle swarm optimization of free parameters for AST construction

	aRP (ms)	floor	*n*	scale	% Total Error
PC run 1	5	0.911	7.234	0.145	11.796
PC run 2	5	0.376	9.919	0.148	11.867
PC run 3	5	0.452	7.791	0.146	11.825
MF run 1	5	1.995	10.000	0.135	12.953
MF run 2	4.8	0.537	9.998	0.131	12.675
MF run 2	5	1.182	9.776	0.131	12.715
MT run 1	5	0.171	2.893	0.147	21.338
MT run 2	5	0.309	2.391	0.119	21.205
MT run 3	5	0.119	2.990	0.119	21.403

Best parameters found in 3 optimization runs and %total error as sum of %deviations of Firing rate, CV, LV, and ISI histogram from recorded spike trains

Table 3 Remaining errors in AST statistics compared to template spike train with and without parameter optimization

	rate	CV	LV	ISI	Total Error
PC opt	−0.01	0.51	2.19	9.37	12.07
PC lb	−15.66	−20.16	−35.33	28.5	140.50
PC ub	−0.02	3.8	2.02	8.84	14.84
PC pl	0.09	−0.8	1.89	11.48	16.33
MF opt	−0.1	0.74	0.15	12.32	13.21
MF lb	−18.98	−24.03	−21.45	37.52	126.28
MF ub	−0.14	2.96	0.1	11.64	15.17
MF pl	0.03	−3.62	−1.09	17.99	24.50
MT opt	−0.54	−0.94	−0.24	17.27	18.45
MT lb	−25.16	−19.69	−17.62	26.69	109.85
MT ub	−0.83	14.5	−0.29	18.03	37.13
MT pl	2.96	0	−4.59	15.38	31.97

Errors are expressed as %deviation from the mean recorded value. The total error is the sum of the absolute 4 individual errors. 'opt' denotes optimal parameters determined with particle swarm algorithm. 'lb' denotes parameters set to lower bounds, 'ub' to upper bounds, and 'pl' denotes our first iteration of parameters set to most plausible physiological values, though 'u' was set somewhat arbitrarily to 8

well at an AST LV of 0.1, but not at an LV of 1.5 (Fig. 8e *vs.* 8f; t = 1–4 s). This indicates that even an average of 100 10–20 Hz highly irregular (LV = 1.5) spike trains cannot match target rate changes at 1–2 Hz smoothly. Mismatches became more prominent when the zap frequency increased (Fig. 8e, f; t = 5–12 s) For each combination of spike rates and LV the match of an average AST aGLR slowly deteriorated as frequency increased. For a zap rate 40–100 Hz the amplitude of sinusoidal rate changes in average aGLRs from ASTs with an LV of 0.1 markedly decreased around 20 Hz (Fig. 8g; t = 3–4 s) and became quite poor at 30–40 Hz (t = 4–5 s). For a spike rate of 10–20 Hz, the average aGLR from ASTs with an LV of 0.1 already diminished around 4 Hz and became quite poor at 8–10 Hz (Fig. 8e). In addition to resulting in mismatches of target rates, sinusoidal rate changes also resulted in an increased error in the LV measured in the resulting ASTs compared to the LV with which gamma intervals were constructed (Table 5). This error was most pronounced when the target LV was 0.1, as the constantly changing rate increased the local variation of the target spike trains in addition to the local variation dictated by the gamma process. As discussed below, these results show limits not only for our method of AST generation, but general limits of how spike trains following a gamma process with a given regularity can code rate changes at different frequencies and how many such spike trains are needed to reliably code a give rate change profile.

3.6 Adding square waveforms to rate templates in order to mimic behavior related rate changes

To examine the ability of our method to introduce controlled rate changes to the template, we added square-wave rate increases and decreases to the rate templates constructed from recordings (Fig. 9). These rate changes were introduced at regular intervals of 5 s or 1 s to mimic a canonical form of rate change that may be associated with a rhythmic behavioral event such as breathing or whisking in a rodent. We then drew a population of ASTs from these rate-modulated templates and constructed peri-event histograms (PSTH) to examine how well ASTs will follow such event-related rate changes. We found that for all of our cell types PC (Fig. 9a, MF

(Fig.9b), MT42 (Fig. 9c), the event aligned ASTs showed rate changes accurately reflecting the imposed canonical behavioral rate change. As can be expected from the preceding analysis using zap templates, the rate change showed a certain amount of low-pass filtering, but was accurately achieving the new target rate within 10–50 ms, with more pronounced low-pass filtering for the cell with the slowest spike rate and highest CV (MT42; Fig. 9c). We further examined the ability of our method to encode smaller or larger spike rate changes related to behavioral events, and found a good ability to accurately reproduce small (Fig. 9d) or large (Fig. 9f) spike rate changes mimicking behavioral events. Populations of spike trains with rate changes introduced at specific times will be specifically useful to provide synaptic input to a neural model in order to study the post-synaptic coding of behavioral events, and its dependence on the proportion of behaviorally modulated spike trains as well as the modulation strength (Abbasi et al. 2017).

4 Discussion

In this report we designed and characterized a new method to construct artificial spike trains that can match single unit recordings obtained in behaving animals. The need for such ASTs arises in two types of studies that address the details of signal integration by single neurons.

First, computer modeling studies of biophysically realistic neuron models require realistic *in vivo*-like input patterns in order to determine their non-linear synaptic integration properties in relevant conditions (Jaeger et al. 1997; Steuber et al. 2011). While one can apply artificial synthetic spike trains with well-defined pairwise correlations purely derived from stochastic processes (Brette 2009; Macke et al. 2009; Niebur 2007), such spike trains do not allow one to systematically vary the rate correlations within subpopulations of ASTs as desired in our studies of single-neuron transfer functions. *Vice versa*, one can directly apply recorded spike trains as input to a model, but a population of recorded spike trains will not contain the rate and spike time correlations converging onto single neurons, and do not allow the flexibility of exploring the

| Table 4 AST statistics with constant rate and LV target				
Target LV	0.1	1.5	0.1	1.5
Target rate (Hz)	1	1	100	100
AST rate(Hz)	0.999 ± 0.0078	0.998 ± 0.048	99.995 ± 0.438	100.3554 ± 2.123
FR error (%)	0.010	0.230	0.0054	0.3554
Surrogate LV	0.1	1.5	0.1	1.5
AST LV	0.1004 ± 0.0052	1.507 ± 0.040	0.099 ± 0.0050	1.4983 ± 0.036
LV error (%)	0.4245	0.5045	1.094	0.114
AST CV	0.262 ± 0.0062	1.410 ± 0.059	0.157 ± 0.0032	0.844 ± 0.032

100 ASTs with refractory period 4 ms were drawn from a constant rate template for analysis

strength of such correlations as an important determinant of postsynaptic neural coding. Our new method of constructing ASTs from rate templates presented here allows the preservation of single spike train statistics of recordings (mean rate, CV, LV), while enabling the manipulation of rate correlations between spike trains as well as their oscillatory and behaviorally event related rate modulation in a highly flexible manner. Our algorithm preserved the rate, CV, and LV properties of all tested spike trains with errors of less than 3%, e.g. a CV of 1.0 could be at worst 0.97 or 1.03 in ASTs. The ISI histogram deviation was in all cases larger than the other errors, and points to a systematic shortcoming of gamma distributed ISIs with a refractory period to completely match the ISI distribution of recorded neurons. However, we are not aware of any other simple stochastic process with a probability density function that would come any closer to the recordings. This ISI histogram mismatch does not come as a big surprise, as previous work for example in Purkinje cell simulations has shown that ISI distributions are shaped by complex activation patterns of voltage-gated conductances (Jaeger and Bower 1999). It is unlikely that a relatively minor mismatch in ISI distributions between ASTs and recorded spike trains leads to differences in the outcome of simulation studies where about a hundred ASTs converge onto a postsynaptic neuron model.

A second important need for populations of *in-vivo* like ASTs arises with the technique of dynamic clamping, where arbitrary excitatory and inhibitory conductance patterns can be applied to neurons recorded with whole-cell patch clamping (Jaeger and Bower 1999; Robinson and Kawai 1993; Sharp et al. 1993). In fact, a direct comparison of modeling a given cell type with dynamic clamping of the same cell type using the same synaptic input patterns also provides a powerful tool to bootstrap the understanding of both modeling and dynamic clamp data (Lin and Jaeger 2011).

A preliminary version of our AST generation method was used in a recent publication studying cerebellar processing (Abbasi et al. 2017), but at that time the method was not thoroughly tested with surrogate data as given in the present report with constant and sine wave modulated rate templates, and the dependence on the choice of free parameters was not ascertained. This testing in the present report led us to tweak a few aspects of the algorithm itself, notably we changed the estimation of a gamma interval from the rate template by not just considering the instantaneous rate at the time of the previous spike, but by considering the average rate over the estimated interval. We also changed the method by which sudden large rate increases can be followed, which was previously given by stopping with a spike at the time of such rate increase and computing the next ISI from the increased rate. That method turned out to create precisely timed spikes at the time of rate increases passing a specific threshold, resulting in spurious rate peaks in PSTH histograms. Our new method also requires the re-estimation of an interval when rate increases clearly indicate a discontinuous rate function, but it combines
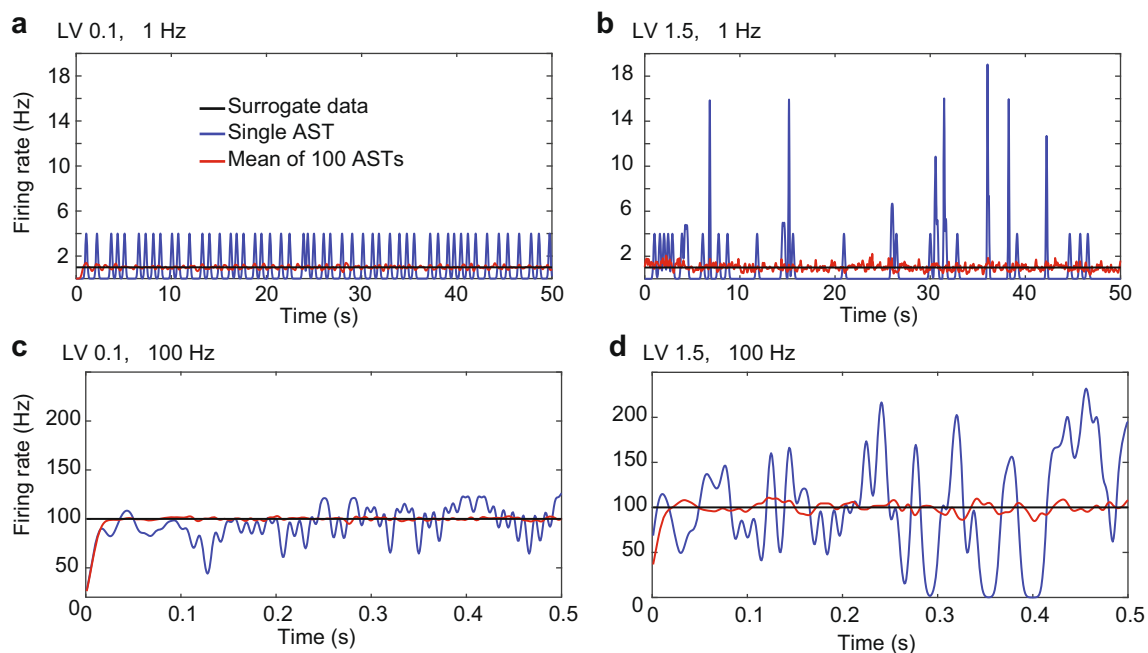
Fig. 7 Constant target rate templates. Surrogate data were constructed as rate templates with a constant target rate and low or high spiking regularity (LV of 0.1 or 1.5). We find that the average spike rate from 100 ASTs matches the target rate with only very small errors (see Table 2). The individual ASTs (blue traces) show large rate fluctuations due to the stochastic nature of the gamma spike train. These random rate fluctuations are much more pronounced for a highly irregular spike train target (**b**, **d**; LV = 1.5) *vs.* a regular spike train target (**a**, **c**). Individual AST rates were constructed as aGLRs with a scale factor (sf, Eq. (4)) of 1.0 instead of 0.25 as used for physiological spike trains in order to more clearly show the contribution of single spikes to rate changes (Fig. 4a, b; blue trace)
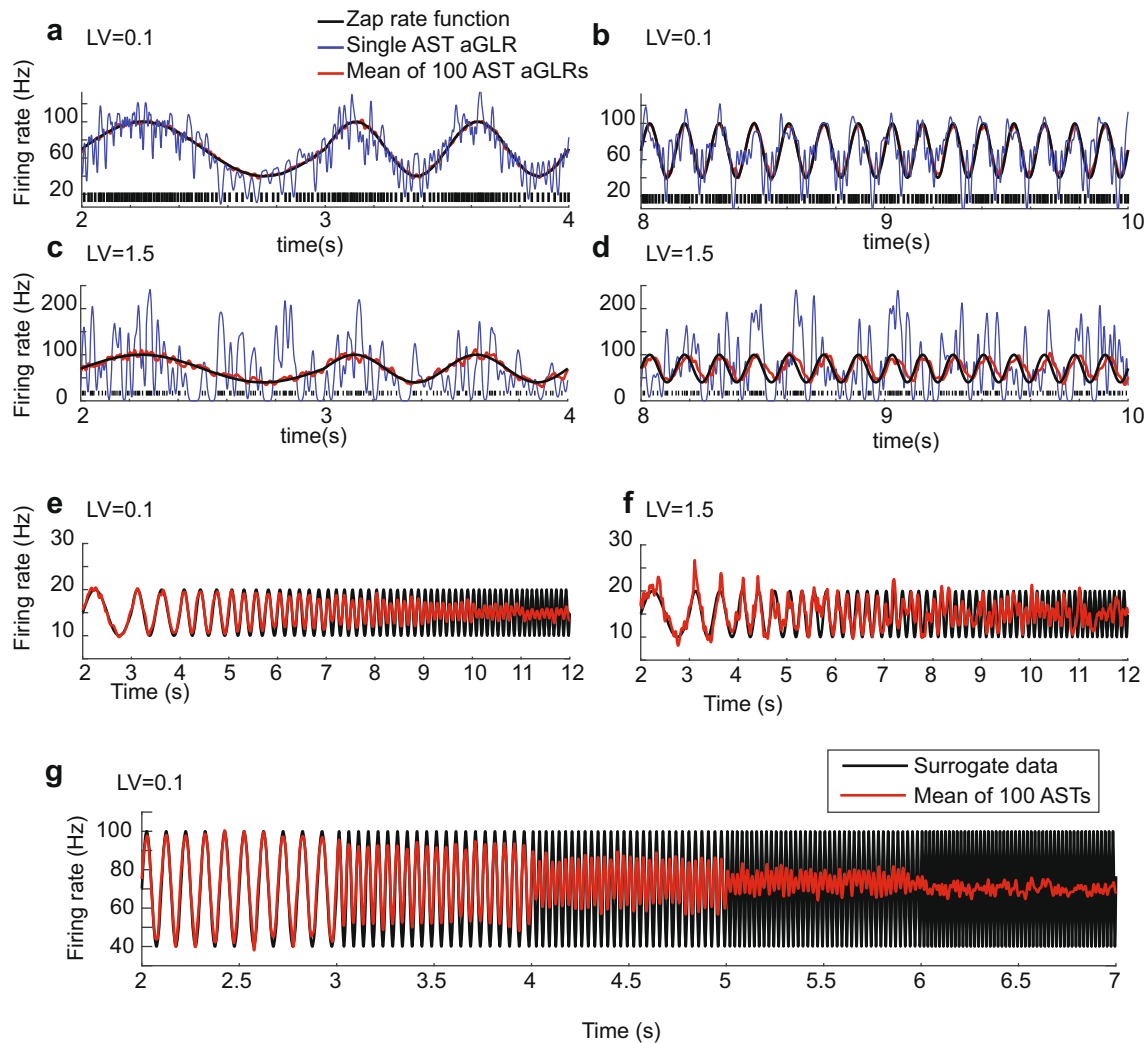
Fig. 8 Sinusoidal target rate templates with increasing frequency (zap). Black traces: Surrogate data were constructed as rate templates with a sinusoidal rate change and increasing frequency, and given a low or high target regularity (LV of 0.1 or 1.5). **a–d** Red traces: Average aGLR of 100 ASTs computed from the target template at low sinusoidal frequencies. A sample AST is depicted with black bars at the bottom of each panel. **e–f** Sinusoidal template (black) and average AST aGLR for higher sinusoidal frequencies and target spike rates of 10–20 Hz (trough and peak of sinusoidal). **g** Same for a target spike rate of 40–100 Hz (trough and peak of sinusoidal) and a regular spike train target (LV = 0.1)

2 successive ISIs with different rate estimates to avoid spurious spike alignment. Our tests with large step-changes in spike rate (Fig. 9) and sinusoidal rate changes with increasing frequency (Fig. 8) of the improved algorithm show that spike rate changes can be followed for spike trains at different mean rates and spike regularity while preserving the statistics of the original spike train. The Matlab code presenting our improved code has now been fully commented and is available

Table 5 Statistics of simulations with zap surrogate rate template

	Zap1to10Hz_min10_max20		Zap1to10Hz_min40_max100		Zap10to100Hz_min10_max20		Zap10to100Hz_min40_max100	
Surrogate FR (Hz)	15	15	70	70	15	15	70	70
ASTs FR (Hz)	15.16 ± 0.302	15.25 ± 1.413	70.39 ± 0.374	71.38 ± 2.133	15.04 ± 0.251	15.08 ± 1.353	71.31 ± 0.419	71.38 ± 2.667
FR error (%)	1.07	1.69	0.56	1.97	0.30	0.52	1.87	1.97
Surrogate LV	0.1	1.5	0.1	1.5	0.1	1.5	0.1	1.5
ASTs LV	0.138 ± 0.016	1.517 ± 0.100	0.124 ± 0.005	1.491 ± 0.038	0.104 ± 0.011	1.516 ± 0.087	0.162 ± 0.008	1.504 ± 0.043
LV error (%)	37.87	1.13	24.29	0.59	3.66	1.09	62.36	0.23
ASTs CV	0.30 ± 0.015	1.33 ± 0.098	0.33 ± 0.007	1.06 ± 0.050	0.25 ± 0.012	1.32 ± 0.108	0.24 ± 0.006	1.01 ± 0.038

as a toolbox for public use along with specific examples as presented in this report https://doi.org/10.15139/S3/8ILYHZ.

In the present implementation of our method we focus on preserving and manipulating rate correlations between ASTs at time scales ranging from 10s of seconds to 10s of milliseconds. Rate correlations at the slow time scale are well documented in brain activity both due to fMRI imaging, where the presence of functional connectivity in frequencies from 0.01 to 0.1 Hz indicates correlated activity changes in brain-wide networks. Such slow rate correlations at the seconds to minute scale have also been confirmed with electrophysiological recordings (Allers et al. 2002; Ruskin et al. 1999a, b) and depend on neuromodulatory input, for example through dopamine (Ruskin et al. 2003). More recently, brain-wide rate changes have been correlated with cholinergic and adrenergic modulation that control alertness, which can be conveniently read out with pupil diameter measurements (Reimer et al. 2016; Shimaoka et al. 2018; Stringer et al. 2018). Pupil diameter additionally is correlated with BOLD activity in fMRI measurements (Murphy et al. 2014; Pisauro et al. 2016; Schneider et al. 2016; Yellin et al. 2015). Rate correlations

on the time scale of seconds to the sub-second range were recently shown in cerebellum as well (Cao et al. 2017), which led to the original formulation of our AST generation method to study synaptic integration in the cerebellar nuclei with modeling (Abbasi et al. 2017). This work also already focused on the introduction of behaviorally related rate changes, which are also correlated between neurons. The functionality of our algorithm allows for the flexible manipulation of rate correlations reflecting the processes listed above in order to determine their influence on synaptic coding in models and dynamic clamping. This relevance remains largely unexplored to date.

Spike time correlations at the millisecond scale are traditionally analyzed with cross-correlation methods (Abeles 1983; Gerstein and Perkel 1969, 1972). In some cases highly precise spike correlations with millisecond precision can be found (Grammont and Riehle 1999), however, the statistical verification of such events occurring at a rate beyond chance remains tricky. Some algorithms of neural computation such as synfire chains (Aertsen et al. 1996; Diesmann et al. 1999) or polychrony (Izhikevich 2006; Izhikevich and Hoppensteadt
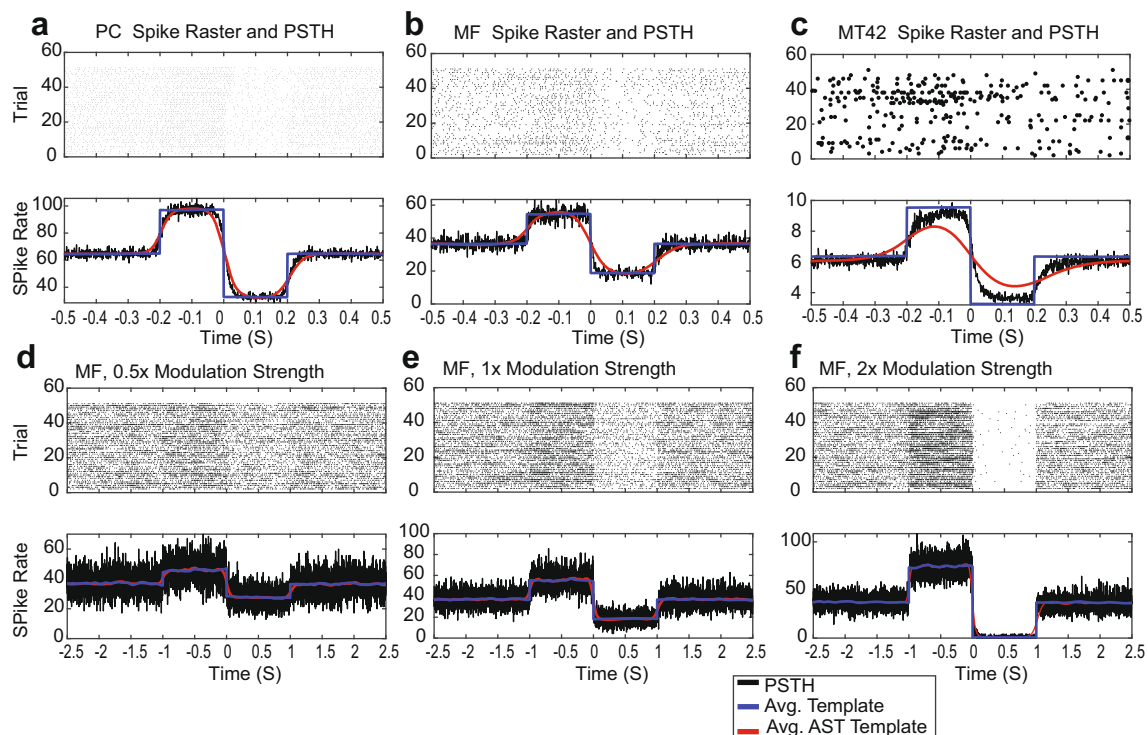
Fig. 9 Physiological spike train templates with superposed rate change events. Rate templates from our 3 sample neuron types were convolved with a square rate change event of 0.4 s (**a**–**c**) or 2 s (**d**–**f**) duration. Square rate changes were $+ - 0.5*$ mean spike rate for a modulation strength of 1 (**a**–**c**, **e**). The rate change was applied to the template at even intervals of 5 s for the 2 s duration rate changes and every 1 s for the 400 ms rate changes. 100 ASTs were constructed from the recorded spike train with the superposed square waveform rate changes, which represent a canonical form of a behavioral event related spike rate change. We then constructed peri-event time histograms (PSTH) aligned to the rate changes. **a**–**f** The top panel shows a raster plot of 50 spike trains aligned to the center of the square rate change. The dot size shown for each spike is scaled to the mean spike rate. The bottom panels show the average rate template around the imposed spike rate change (blue traces), which is the target rate for the ASTs. Black trace: The mean spike rate per 1 ms bin of all event aligned spike trains ($N = 11,200$ [2100] for PC, $N = 4400$ [900] for MF, and $N = 107,900$ [21,600] for MT42), where [] brackets denote the event numbers for panels d-f. Red traces: Mean event aligned aGLR constructed from the ASTs

2009) require millisecond precise spike alignment, but their implementation in the brain remains largely unsubstantiated. In contrast, neural networks can compute behaviorally relevant information purely on rate coding principles (Bobier et al. 2014; Eliasmith et al. 2012; Stewart et al. 2012), and rate coding remains the dominant interpretation of neural computation in cortex. On the other hand, some highly specialized neural systems clearly can employ a precise spike time code, such as auditory sound localization in the inferior colliculus (Wagner et al. 1987) or millisecond precision of error signals provided by the inferior olive to the cerebellum (Lang et al. 1999; Ozden et al. 2009; Welsh et al. 1995). Our algorithm as presently implemented does not allow for the insertion of millisecond precise spike events across spike trains because all ISIs are drawn in a stochastic manner from a gamma distribution. As shown in Figs. 8 and 9, this limits spike rate change correlations to above the millisecond scale, and leads to low-pass filtering of fast rate changes. Our results demonstrate this important limitation of stochastic processes with spike rates of 1–100 Hz and realistic CVs of 0.1–1.5 of following faster rate change signals (Fig. 8). However, the algorithm could be extended to include precisely aligned spikes in at least two ways. First, synchronized spikes could be inserted as an independent set of events into our ASTs while removing the nearest neighboring spike. Second, more sophisticated mixture methods (Brette 2009) could be employed to copy spikes between source spike trains, which would be our ASTs without precise spike alignment in this case. Employing such refinements will be desirable for reflecting special fast cases of neural processing such as gap junction coupling (Traub et al. 2001), auditory sound localization (Wagner et al. 1987), or synchronization in networks of coupled oscillators (Lewis and Rinzel 2003).

Compliance with ethical standards

Conflict of interest The authors declare that they have no conflict of interest.

References

Abbasi, S., Hudson, A. E., Maran, S. K., Cao, Y., Abbasi, A., Heck, D. H., & Jaeger, D. (2017). Robust transmission of rate coding in the inhibitory Purkinje cell to cerebellar nuclei pathway in awake mice. *PLoS Computational Biology, 13*.

Abeles, M. (1983). The quantification and graphic display of correlations among three spike trains. *IEEE Transactions on Biomedical Engineering, BME-30*, 235–239.

Aertsen, A., Diesmann, M., & Gewaltig, M. O. (1996). Propagation of synchronous spiking activity in feedforward neural networks. *Journal of Physiology (Paris), 90*, 243–247.

Allers, K. A., Ruskin, D. N., Bergstrom, D. A., Freeman, L. E., Ghazi, L. J., Tierney, P. L., & Walters, J. R. (2002). Multisecond periodicities in basal ganglia firing rates correlate with theta bursts in transcortical and hippocampal EEG. *J.Neurophysiol., 87*, 1118–1122.

Bobier, B., Stewart, T. C., & Eliasmith, C. (2014). A unifying mechanistic model of selective attention in spiking neurons. *PLoS Computational Biology, 10*.

Brette, R. (2009). Generation of correlated spike trains. *Neural Computation, 21*, 188–215.

Brown, J., Pan, W. X., & Dudman, J. T. (2014). The inhibitory microcircuit of the substantia nigra provides feedback gain control of the basal ganglia output. *Elife, 3*, e02397.

Cao, Y., Liu, Y., Jaeger, D., & Heck, D. H. (2017). Cerebellar Purkinje cells generate highly correlated spontaneous slow-rate fluctuations. *Frontiers in Neural Circuits, 11*, 67.

Cui, Y., Liu, L. D., Khawaja, F. A., Pack, C. C., & Butts, D. A. (2013). Diverse suppressive influences in area MT and selectivity to complex motion features. *The Journal of Neuroscience, 33*, 16715–16728.

Diesmann, M., Gewaltig, M. O., & Aertsen, A. (1999). Stable propagation of synchronous spiking in cortical neural networks. *Nature, 402*, 529–533.

Edgerton, J. R., Hanson, J. E., Gunay, C., & Jaeger, D. (2010). Dendritic sodium channels regulate network integration in Globus Pallidus neurons: A modeling study. *The Journal of Neuroscience, 30*, 15146–15159.

Eliasmith, C., Stewart, T. C., Choo, X., Bekolay, T., DeWolf, T., Tang, Y., & Rasmussen, D. (2012). A large-scale model of the functioning brain. *Science, 338*, 1202–1205.

Gerstein, G. L., & Perkel, D. H. (1969). Simultaneously recorded trains of action potentials: Analysis and functional interpretation. *Science, 164*, 828–830.

Gerstein, G. L., & Perkel, D. H. (1972). Mutual temporal relationships among neuronal spike trains statistical techniques for display and analysis. *Biophys.J., 12*, 453–473.

Grammont, F., & Riehle, A. (1999). Precise spike synchronization in monkey motor cortex involved in preparation for movement. *Experimental Brain Research, 128*, 118–122.

Gutnisky, D. A., & Josic, K. (2010). Generation of spatiotemporally correlated spike trains and local field potentials using a multivariate autoregressive process. *Journal of Neurophysiology, 103*, 2912–2930.

Hutcheon, B., & Yarom, Y. (2000). Resonance, oscillation and the intrinsic frequency preferences of neurons. *Trends in Neurosciences, 23*, 216–222.

Izhikevich, E. M. (2006). Polychronization: Computation with spikes. *Neural Computation, 18*, 245–282.

Izhikevich, E. M., & Hoppensteadt, F. C. (2009). Polychronous wavefront computations. *International Journal of Bifurcation and Chaos, 19*, 1733–1739.

Jaeger, D., & Bower, J. M. (1999). Synaptic control of spiking in cerebellar Purkinje cells: Dynamic current clamp based on model conductances. *The Journal of Neuroscience, 19*, 6090–6101.

Jaeger, D., DeSchutter, E., & Bower, J. M. (1997). The role of synaptic and voltage-gated currents in the control of Purkinje cell spiking: A modeling study. *The Journal of Neuroscience, 17*, 91–106.

Jun, J. J., Steinmetz, N. A., Siegle, J. H., Denman, D. J., Bauza, M., Barbarits, B., Lee, A. K., Anastassiou, C. A., Andrei, A., Aydin, C., et al. (2017). Fully integrated silicon probes for high-density recording of neural activity. *Nature, 551*, 232–236.

Krumin, M., & Shoham, S. (2009). Generation of spike trains with controlled auto- and cross-correlation functions. *Neural Computation, 21*, 1642–1664.

Lang, E. J., Sugihara, I., Welsh, J. P., & Llinas, R. (1999). Patterns of spontaneous Purkinje cell complex spike activity in the awake rat. *The Journal of Neuroscience, 19*, 2728–2739.

Ledergerber, D., & Larkum, M. E. (2010). Properties of layer 6 pyramidal neuron apical dendrites. *The Journal of Neuroscience, 30*, 13031–13044.

Lewis, T. J., & Rinzel, J. (2003). Dynamics of spiking neurons connected by both inhibitory and electrical coupling. *Journal of Computational Neuroscience, 14*, 283–309.

Lin, R. J., & Jaeger, D. (2011). Using computer simulations to determine the limitations of dynamic clamp stimuli applied at the soma in mimicking distributed conductance sources. *Journal of Neurophysiology, 105*, 2610–2624.

Lyamzin, D. R., Macke, J. H., & Lesica, N. A. (2010). Modeling population spike trains with specified time-varying spike rates, trial-to-trial variability, and pairwise signal and noise correlations. *Frontiers in Computational Neuroscience, 4*, 144.

Lyamzin, D. R., Barnes, S. J., Donato, R., Garcia-Lazaro, J. A., Keck, T., & Lesica, N. A. (2015). Nonlinear transfer of signal and noise correlations in cortical networks. *The Journal of Neuroscience, 35*, 8065–8080.

Macke, J. H., Berens, P., Ecker, A. S., Tolias, A. S., & Bethge, M. (2009). Generating spike trains with specified correlation coefficients. *Neural Computation, 21*, 397–423.

Major, G., Larkum, M. E., & Schiller, J. (2013). Active properties of neocortical pyramidal neuron dendrites. *Annual Review of Neuroscience, 36*, 1–24.

Marre, O., El Boustani, S., Frégnac, Y., & Destexhe, A. (2009). Prediction of spatiotemporal patterns of neural activity from pairwise correlations. *Physical Review Letters, 102*.

Mel, B. W. (1993). Synaptic integration in an excitable dendritic tree. *Journal of Neurophysiology, 70*, 1086–1101.

Miura, K., Okada, M., & Amari, S. I. (2006). Estimating spiking irregularities under changing environments. *Neural Computation, 18*, 2359–2386.

Murphy, B. K., & Miller, K. D. (2003). Multiplicative gain changes are induced by excitation or inhibition alone. *The Journal of Neuroscience, 23*, 10040–10051.

Murphy, P. R., O'Connell, R. G., O'Sullivan, M., Robertson, I. H., & Balsters, J. H. (2014). Pupil diameter Covaries with BOLD activity in human locus Coeruleus. *Human Brain Mapping, 35*, 4140–4154.

Niebur, E. (2007). Generation of synthetic spike trains with defined pairwise correlations. *Neural Computation, 19*, 1720–1738.

Ozden, I., Sullivan, M. R., Lee, H. M., & Wang, S. S. H. (2009). Reliable coding emerges from Coactivation of climbing fibers in microbands of cerebellar Purkinje neurons. *The Journal of Neuroscience, 29*, 10463–10473.

Paulin, M. G., & Hoffman, L. F. (2001). Optimal firing rate estimation. *Neural Networks, 14*, 877–881.

Pillow, J. W., Shlens, J., Paninski, L., Sher, A., Litke, A. M., Chichilnisky, E. J., & Simoncelli, E. P. (2008). Spatio-temporal correlations and visual signalling in a complete neuronal population. *Nature, 454*, 995–999.

Pipa, G., Grün, S., & van Vreeswijk, C. (2013). Impact of spike train autostructure on probability distribution of joint spike events. *Neural Computation, 25*, 1123–1163.

Pisauro, M. A., Benucci, A., & Carandini, M. (2016). Local and global contributions to hemodynamic activity in mouse cortex. *Journal of Neurophysiology, 115*, 2931–2936.

Poirazi, P., Brannon, T., & Mel, B. W. (2003). Arithmetic of subthreshold synaptic summation in a model CA1 pyramidal cell. *Neuron, 37*, 977–987.

Polsky, A., Mel, B., & Schiller, J. (2009). Encoding and decoding bursts by NMDA spikes in basal dendrites of layer 5 pyramidal neurons. *The Journal of Neuroscience, 29*, 11891–11903.

Prinz, A. A., Bucher, D., & Marder, E. (2004). Similar network activity from disparate circuit parameters. *Nature Neuroscience, 7*, 1345–1352.

Reimer, J., McGinley, M. J., Liu, Y., Rodenkirch, C., Wang, Q., McCormick, D. A., & Tolias, A. S. (2016). Pupil fluctuations track rapid changes in adrenergic and cholinergic activity in cortex. *Nature Communications, 7*, 13289.

Robinson, H. P. C., & Kawai, N. (1993). Injection of digitally synthesized synaptic conductance transients to measure the integrative properties of neurons. *Journal of Neuroscience Methods, 49*, 157–165.

Ruskin, D. N., Bergstrom, D. A., Kaneoke, Y., Patel, B. N., Twery, M. J., & Walters, J. R. (1999a). Multisecond oscillations in firing rate in the basal ganglia: Robust modulation by dopamine receptor activation and anesthesia. *Journal of Neurophysiology, 81*, 2046–2055.

Ruskin, D. N., Bergstrom, D. A., & Walters, J. R. (1999b). Multisecond oscillations in firing rate in the globus pallidus: Synergistic modulation by D1 and D2 dopamine receptors. *The Journal of Pharmacology and Experimental Therapeutics, 290*, 1493–1501.

Ruskin, D. N., Bergstrom, D. A., Tierney, P. L., & Walters, J. R. (2003). Correlated multisecond oscillations in firing rate in the basal ganglia: Modulation by dopamine and the subthalamic nucleus. *Neuroscience, 117*, 427–438.

Schneider, M., Hathway, P., Leuchs, L., Samann, P. G., Czisch, M., & Spoormaker, V. I. (2016). Spontaneous pupil dilations during the resting state are associated with activation of the salience network. *Neuroimage, 139*, 189–201.

Sharp, A. A., Oneil, M. B., Abbott, L. F., & Marder, E. (1993). Dynamic clamp - computer-generated Conductances in real neurons. *Journal of Neurophysiology, 69*, 992–995.

Shimaoka, D., Harris, K. D., & Carandini, M. (2018). Effects of arousal on mouse sensory cortex depend on modality. *Cell Reports, 22*, 3160–3167.

Shimaoka, D., Steinmetz, N. A., Harris, K. D., & Carandini, M. (2019). The impact of bilateral ongoing activity on evoked responses in mouse cortex. *Elife*, 8.

Shinomoto, S., Shima, K., & Tanji, J. (2003). Differences in spiking patterns among cortical neurons. *Neural Computation, 15*, 2823–2842.

Shinomoto, S., Miura, K., & Koyama, S. (2005). A measure of local variation of inter-spike intervals. *Biosystems, 79*, 67–72.

Silver, R. A. (2010). Neuronal arithmetic. *Nature Reviews Neuroscience, 11*, 474–489.

Steuber, V., Schultheiss, N. W., Silver, R. A., De Schutter, E., & Jaeger, D. (2011). Determinants of synaptic integration and heterogeneity in rebound firing explored with data driven models of deep cerebellar nucleus cells. *Journal of Computational Neuroscience, 30*, 633–658.

Stewart, T. C., Bekolay, T., & Eliasmith, C. (2012). Learning to select actions with spiking neurons in the basal ganglia. *Frontiers in Neuroscience, 6*, 2.

Stringer, C., Pachitariu, M., Steinmetz, N., Bai Reddy, C., Carandini, M., & Harris, K. D. (2018). Spontaneous behaviors drive multidimensional, brain-wide population activity. *bioRxiv*.

Stringer, C., Pachitariu, M., Steinmetz, N., Reddy, C. B., Carandini, M., & Harris, K. D. (2019). Spontaneous behaviors drive multidimensional, brainwide activity. *Science, 364*, 255.

Traub, R. D., Kopell, N., Bibbig, A., Buhl, E. H., LeBeau, F. E., & Whittington, M. A. (2001). Gap junctions between interneuron dendrites can enhance synchrony of gamma oscillations in distributed networks. *The Journal of Neuroscience, 21*, 9478–9486.

Wagner, H., Takahashi, T., & Konishi, M. (1987). Representation of interaural time difference in the central nucleus of the barn owl's inferior colliculus. *J.Neurosci., 7*, 3105–3116.

Wagner, M. J., Kim, T. H., Kadmon, J., Nguyen, N. D., Ganguli, S., Schnitzer, M. J., & Luo, L. (2019). Shared cortex-cerebellum

dynamics in the execution and learning of a motor task. *Cell.*, *177*, 669–682. e24.

Welsh, J. P., Lang, E. J., Suglhara, I., & Llinas, R. (1995). Dynamic organization of motor control within the olivocerebellar system. *Nature, 374*, 453–457.

Yellin, D., Berkovich-Ohana, A., & Malach, R. (2015). Coupling between pupil fluctuations and resting-state fMRI uncovers a slow build-up of antagonistic responses in the human cortex. *Neuroimage, 106*, 414–427.